

Robust Picosecond writing of a Layered Antiferromagnet by Staggered Spin-Orbit-Fields

P. E. Roy,^{1,*} R. M. Otxoa,^{1,†} and J. Wunderlich^{1,2}

¹*Hitachi Cambridge Laboratory, J J Thomson Avenue, Cambridge CB3 0HE, UK*

²*Institute of Physics ASCR, v.v.i., Cukrovarnicka 10, 162 53 Praha 6, Czech Republic*

(Dated: April 21, 2016)

Ultrafast electrical switching by current-induced staggered spin-orbit fields, with minimal risk of overshoot, is shown in layered easy-plane antiferromagnets with basal-plane biaxial anisotropy. The reliable switching is due to the field-like torque, relaxing stringent requirements with respect to precision in the time-duration of the excitation pulse. We investigate the switching characteristics as a function of the spin-orbit field strength, pulse duration, pulse rise and fall time and damping by atomistic spin dynamics simulations and an effective equation of motion for the antiferromagnetic order-parameter. The condition, determining the critical spin-orbit field strength for switching is determined and we go on to show that robust picosecond writing is possible at feasible current magnitudes.

PACS numbers: 75.78.Jp, 75.60.Jk, 75.50.Ee, 75.10.Hk

The inherent properties of antiferromagnets (AFMs) such as ultrafast dynamics, zero net moment and insensitivity to external magnetic stray fields, make them candidates for a new generation of high speed memory devices. The fact that AFMs also exhibit anisotropic magnetoresistance makes it possible to detect the AFM state by electrical means. The writing operation, i.e. reorientation of the AFM sublattice magnetizations has been subject to several proposals, which includes using short laser pulses [1–3] and spin transfer torque (STT) induced by an impinging spin accumulation generated either by the spin hall effect at a heavy metal/AFM interface [4] or by injection from a coupled ferromagnet [5, 6]. In those electrical techniques, the spin-accumulation with polarization \mathbf{p} causes a staggered field on the AFM sublattices A and B (the staggered nature being what couples effectively to the AFM order parameter) of the form $\mathbf{H}_{(A,B)} \sim \mathbf{m}_{(A,B)} \times \mathbf{p}$. The resulting torque is thus of antidamping type and unless care is taken with respect to pulse duration, an overshoot is a viable risk [4] as the torque is turned on at all times that the current is on. Furthermore, several theoretical studies focus on driving AFM domain walls (DWs) by means of STT [7–10]. These works have been important in predicting the possibility of current-induced excitations in AFMs. However, unless the type of DWs considered in those works can be controllably formed and their position easily detected, it is as of now, difficult to conceive of a device with moving AFM DWs as the mode of operation. For a robust device, electrical manipulation whereby the AFM order parameter is switched fast and controllably between two stable minima, without the need for any coupled FMs is a desirable route to follow.

In crystals with locally broken inversion-symmetry at the magnetic sites and where A and B form inversion partners, another mechanism for AFM spin-axis reorientation presents itself as proposed in ref [11]. There,

the inverse spin galvanic effect [12] produces a local non-equilibrium spin polarization, alternating in sign between sublattices A and B , thus generating a staggered spin-orbit (SO) field, \mathbf{H}^{SO} , which does not depend on $\mathbf{m}_{(A,B)}$. \mathbf{H}^{SO} leads then to a field-like torque on $\mathbf{m}_{(A,B)}$. These conditions can be generated by an electrical current density \mathbf{j} , injected perpendicular to the axis of locally broken inversion symmetry. Proposed materials to this end are to date Mn_2Au and CuMnAs [11, 13–20]. Experimental indication of the electrical manipulation of the AFM state in a multidomain CuMnAs sample has recently been reported [19].

In this work, we show reliable ultrafast switching of a Mn_2Au device whose body centered tetragonal crystal structure [21] is shown Fig. 1(a). This system exhibits a magnetically hard-axis along the c -axis and has a biaxial anisotropy in the basal-planes with easy directions along the $[110]$ and $[1\bar{1}0]$ axes [11, 22]. Mn atoms occupy sublattices A and B (Fig. 1(a)). Typical basal-plane domain sizes in Mn_2Au is according to ref [20] ~ 500 nm. Thus for a homogeneous Neel ordered state the lateral dimensions of a thin film device should be smaller than this. A current injected parallel to the basal planes generates a staggered SO-field, alternating in sign as $\mathbf{H}_A^{\text{SO}} \sim +\hat{\mathbf{z}} \times \mathbf{j}$ (at sublattice A) and $\mathbf{H}_B^{\text{SO}} \sim -\hat{\mathbf{z}} \times \mathbf{j}$ (at sublattice B). The resulting torques are therefore field-like. To effectively switch the spin-axes of the sublattices between two stable minima, the biaxial easy directions should coincide with the current-directions. We thus consider the geometry in Fig. 1(b) [11]. Recent calculated values of $|\mathbf{H}^{\text{SO}}|$ for Mn_2Au is ~ 20 Oe per 10^7 A/cm² (slightly lower than for CuMnAs) [19].

For modeling the device, the total energy, comprised of exchange, tetragonal anisotropy and Zeeman energies

is :

$$\begin{aligned}
 E = & - \sum_{i,j \in N_i} J_{ij} \mathbf{m}_i \cdot \mathbf{m}_j - K_{2\perp} \sum_i (\mathbf{m}_i \cdot \hat{\mathbf{u}}_3)^2 \\
 & - \frac{K_{4\perp}}{2} \sum_i (\mathbf{m}_i \cdot \hat{\mathbf{u}}_3)^4 - \frac{K_{4\parallel}}{2} \sum_i (\mathbf{m}_i \cdot \hat{\mathbf{u}}_1)^4 \\
 & - \frac{K_{4\parallel}}{2} \sum_i (\mathbf{m}_i \cdot \hat{\mathbf{u}}_2)^4 - \mu_0 \mu_s \sum_i \mathbf{m}_i \cdot \mathbf{H}_i^{\text{SO}}
 \end{aligned} \quad (1)$$

where \mathbf{m} is the unit magnetic moment, μ_0 the magnetic permeability in vacuum and μ_s the saturation magnetic moment. The first term in Eq. (1) is the exchange energy with coupling constants J_{ij} between moments i and j . Terms two, three and four constitute the magnetocrystalline anisotropy energy with $K_{2\perp}$, $K_{4\perp}$ and $K_{4\parallel}$ being the second order perpendicular, fourth order perpendicular and fourth order in-plane anisotropy constants, respectively. Unit vectors $\hat{\mathbf{u}}_{1,2,3}$ denote easy directions. Furthermore, \mathbf{H}_i^{SO} is the current-induced staggered magnetic SO-field.

The equation of motion at each site for \mathbf{m}_i in the precess of the interaction fields \mathbf{H}_i is given by the Landau-Lifshitz-Gilbert equation:

$$(1 + \alpha^2) \frac{\partial \mathbf{m}_i}{\partial t} = -\gamma \mathbf{m}_i \times \mathbf{H}_i - \alpha \gamma \mathbf{m}_i \times (\mathbf{m}_i \times \mathbf{H}_i). \quad (2)$$

Here, γ is the gyromagnetic ratio, α is the damping parameter and \mathbf{H}_i is evaluated from Eq. (1) as $\mathbf{H}_i = \frac{-1}{\mu_0 \mu_s} \frac{\partial E_i}{\partial \mathbf{m}_i}$. We start out by trying the switching capability of the device in Fig. 1(b) using atomistic spin dynamics simulations [23]. The simulation is carried out for a device of size $150 \times 150 \times 5$ unit cells ($49.2 \times 49.2 \times 4.2695$ nm³) of the crystal shown in Fig. 1(a). The exchange constants used are $J_1 = -396 k_B^{-1}$ K, $J_2 = -532 k_B^{-1}$ K and $J_3 = 115 k_B^{-1}$ K [13, 15, 24] where k_B is the Boltzmann constant. For the biaxial basal-plane-anisotropy, $K_{4\parallel}$ corresponds to an anisotropy field of 100 Oe, as deduced from experiments in ref. [15]; $K_{4\parallel}$ is here then 1.8548×10^{-25} J. $K_{2\perp}$ and $K_{4\perp}$ per Mn-ion is taken from calculated values in ref [14]. We set here $K_{2\perp} = -1.303 \times 10^{-22}$ J and use the ratio $K_{4\perp} = 2K_{4\parallel}$ [14]. Here, $\alpha = 0.01$ and the Mn magnetic moment, $\mu_s = 4\mu_b$ [15], where μ_b is the Bohr magneton. Considering the device in Fig. 1(b), $\hat{\mathbf{u}}_1 = \hat{\mathbf{x}}$, $\hat{\mathbf{u}}_2 = \hat{\mathbf{y}}$ and $\hat{\mathbf{u}}_3 = \hat{\mathbf{z}}$. Eq. (2) is then solved by a fifth order Runge-Kutta scheme [26]. The first trial consists in applying two current pulses: the first pulse aims to switch the A (B) sublattice from being parallel (antiparallel) to $\hat{\mathbf{x}}$ into directions parallel (antiparallel) to $\hat{\mathbf{y}}$ and the second pulse to switch the sublattices back to their original state. The procedure is as follows: a $\tau_p = 20$ ps long square current pulse is sent along $+\hat{\mathbf{x}}$, generating a staggered \mathbf{H}^{SO} along $+\hat{\mathbf{y}}$ on an A-site and along $-\hat{\mathbf{y}}$ on a B-site. A waiting time of 15 ps is then imposed to verify the stability of the written state. Then a second current pulse along $-\hat{\mathbf{y}}$ is

applied, thus generating a staggered \mathbf{H}^{SO} which is parallel (antiparallel) to $\hat{\mathbf{x}}$ on A (B)-sites. We set $|\mathbf{H}^{\text{SO}}| = 100$ Oe, corresponding to $\sim 5 \times 10^7$ A/cm². To characterize the state, we use the antiferromagnetic order parameter $\mathbf{l} = \frac{\mathbf{m}_A - \mathbf{m}_B}{2}$ and the magnetization $\mathbf{m} = \frac{\mathbf{m}_A + \mathbf{m}_B}{2}$. As the system is three-dimensional, the volume averaged \mathbf{l} and \mathbf{m} are extracted. As can be seen in Fig. 1(c), the switch-

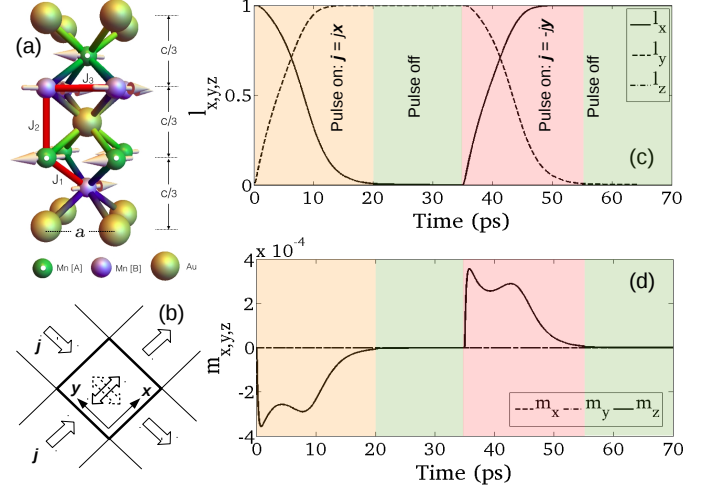


FIG. 1. (Color online) (a): Crystal and spin structure of Mn₂Au with basal-plane lattice parameter $a = 3.328$ Å, $c = 8.539$ Å. The bond-exchange constants $J_{1,2,3}$ used are marked by red solid lines. The Mn atoms occupy two types of sites, A and B (see the key). (b): Coordinate system and orientation of a square device. Current (\mathbf{j}) injection-directions are indicated by large hollow arrows and two stable positions of the antiferromagnetic sublattices are shown by double arrows in the device. $+\hat{\mathbf{z}}$ is along the outward paper normal. (c) and (d): Atomistic spin dynamics results of the time evolution of \mathbf{l} (c) and \mathbf{m} (d) during two writing operations as described in the text.

ing cycle is successful and shows no overshoot in this case. Further, due to the symmetry of the torques, l_z , m_x and m_y remain zero at all times. As the SO-torque itself is not staggered, a build-up in m_z occurs (Fig. 1(d)) causing a large precessional exchange torque (first term in Eq. (2)) along the $\pm\hat{\mathbf{y}}$ -directions. Fast switching is therefore the result of an exchange-enhanced torque. The damping exchange-torque (second term in Eq.(2)) acts as to restore m_z to zero, i.e., the lower the α , the larger the amplitude of m_z , which result in shorter switching times and lower SO-fields required to achieve a switch. Note here that we have used a quite long τ_p . In order to achieve a switch, τ_p need only to be long enough to bring \mathbf{l} over the biaxial anisotropy barrier, after which even if the pulse is off, the biaxial anisotropy field brings \mathbf{l} to the next stable minima. The simulation in Figs. 1(c,d) also show that even though τ_p was on for a time longer than that required to cause a switch, \mathbf{l} did not overshoot the targeted minimum. The reason is that the SO-torque is field-like and the direction of \mathbf{H}^{SO} is always along an

easy direction for the geometry in Fig. (1b). Thus even for a DC current, \mathbf{l} is unlikely to overshoot the targeted anisotropy minima. There may be, however, some conditions, whereby an overshoot event could occur. We therefore firstly investigate the dependence of the final orientation of \mathbf{l} for different τ_p and $|\mathbf{H}^{\text{SO}}|$ at different values of α during a switching event. For this, a simplified model allows large sweeps in parameter space at low computational cost: Thus, we consider a macrospin description where the system consist of two homogeneous antiferromagnetically coupled sublattices carrying total moments \mathbf{m}_A and \mathbf{m}_B . The current-induced SO-field is then \mathbf{H}^{SO} at \mathbf{m}_A and $-\mathbf{H}^{\text{SO}}$ at \mathbf{m}_B . Setting $J_{ij} < 0$, $K_{2\perp} < 0$ and using the Gilbert equation, the coupled equations of motion for \mathbf{m}_A and \mathbf{m}_B are:

$$\begin{aligned} \dot{\mathbf{m}}_A = & \omega_e [\mathbf{m}_A \times \mathbf{m}_B] + \omega_{2\perp} m_{A,z} [\mathbf{m}_A \times \hat{\mathbf{z}}] \\ & - \omega_{4\perp} m_{A,z}^3 [\mathbf{m}_A \times \hat{\mathbf{z}}] - \omega_{4\parallel} m_{A,x}^3 [\mathbf{m}_A \times \hat{\mathbf{x}}] \\ & - \omega_{4\parallel} m_{A,y}^3 [\mathbf{m}_A \times \hat{\mathbf{y}}] - \gamma [\mathbf{m}_A \times \mathbf{H}^{\text{SO}}] \\ & + \alpha \mathbf{m}_A \times \dot{\mathbf{m}}_A \end{aligned} \quad (3)$$

$$\begin{aligned} \dot{\mathbf{m}}_B = & -\omega_e [\mathbf{m}_A \times \mathbf{m}_B] + \omega_{2\perp} m_{B,z} [\mathbf{m}_B \times \hat{\mathbf{z}}] \\ & - \omega_{4\perp} m_{B,z}^3 [\mathbf{m}_B \times \hat{\mathbf{z}}] - \omega_{4\parallel} m_{B,x}^3 [\mathbf{m}_B \times \hat{\mathbf{x}}] \\ & - \omega_{4\parallel} m_{B,y}^3 [\mathbf{m}_B \times \hat{\mathbf{y}}] + \gamma [\mathbf{m}_B \times \mathbf{H}^{\text{SO}}] \\ & + \alpha \mathbf{m}_B \times \dot{\mathbf{m}}_B. \end{aligned} \quad (4)$$

Here, $\omega_e = \frac{2\gamma|J|}{\mu_0\mu_s}$ with $|J| = |4J_1 + J_2|$, $\omega_{2\perp} = \frac{2\gamma|K_{2\perp}|}{\mu_0\mu_s}$, $\omega_{4\perp} = \frac{2\gamma K_{4\perp}}{\mu_0\mu_s}$ and $\omega_{4\parallel} = \frac{2\gamma K_{4\parallel}}{\mu_0\mu_s}$ while the dot denotes the time-derivative. \mathbf{l} and the total magnetization \mathbf{m} are defined as before. It follows that $\mathbf{m} \cdot \mathbf{l} = 0$ and $|\mathbf{l}|^2 + |\mathbf{m}|^2 = 1$. Due to strong exchange interaction, we take the exchange limit, $|\mathbf{m}| \ll |\mathbf{l}|$. Then, $l^2 \approx 1$ and $\mathbf{l} \cdot \dot{\mathbf{l}} \approx 0$. The system is describable by $\mathbf{m} = (0, 0, m_z)$ and $\mathbf{l} = (l_x, l_y, 0)$ (verified e.g in Fig. 1(c,d)). Combining Eqs.(3)-(4) and neglecting the second-order damping terms $\alpha \mathbf{m} \times \dot{\mathbf{m}}$, $\alpha \mathbf{m} \times \dot{\mathbf{l}}$ and $\alpha \mathbf{l} \times \dot{\mathbf{m}}$ in combination with $|\omega_e| \gg |\omega_{2\perp}|$, $|\omega_{4\perp}|$, $|\omega_{4\parallel}|$, $|\gamma \mathbf{l} \cdot \mathbf{H}^{\text{SO}}|$, one arrives at $\mathbf{m} \approx -\frac{1}{2\omega_e} \mathbf{l} \times \dot{\mathbf{l}}$ and consequently:

$$\mathbf{l} \times \{\ddot{\mathbf{l}} - \omega_R^2 [l_x^3 \hat{\mathbf{x}} + l_y^3 \hat{\mathbf{y}}] - 2\omega_e \gamma \mathbf{H}^{\text{SO}} + 2\omega_e \alpha \dot{\mathbf{l}}\} \approx 0, \quad (5)$$

where $\omega_R = \sqrt{2\omega_e \omega_{4\parallel}}$. In planar cylindrical coordinates $(l_x, l_y) = (\cos\phi, \sin\phi)$ the non-rivial solution of Eq.(5) is found by solving :

$$\ddot{\phi} + \frac{\omega_R^2}{4} \sin(4\phi) - 2\omega_e \gamma (H_y^{\text{SO}} \cos\phi - H_x^{\text{SO}} \sin\phi) + 2\omega_e \alpha \dot{\phi} = 0, \quad (6)$$

where, if $\mathbf{j} \parallel \hat{\mathbf{x}}$, then $\mathbf{H}^{\text{SO}} = H_y^{\text{SO}} \hat{\mathbf{y}}$ and if $\mathbf{j} \parallel -\hat{\mathbf{y}}$ then $\mathbf{H}^{\text{SO}} = H_x^{\text{SO}} \hat{\mathbf{x}}$. Here, $m_z \approx -\frac{1}{2\omega_e} \dot{\phi}$. We have in Figs. 2(a-f) included an example of a comparison between the macrospin description (Eqs.(3)-(4)), Eq. (6) and full atomistic spin dynamics simulations. There, a low $\alpha = 0.001$, $\tau_p = 3$ ps and $|\mathbf{H}^{\text{SO}}| = 40$ Oe (close to the

limit of a successful switch) was used as a severe test. Two cases were considered in the atomistic spin dynamics simulations; a finite sized device (same size as that used for the results in Fig. 1(c,d)) and periodic boundary conditions (PBC) along x, y, z still with $150 \times 150 \times 5$ unit cells. Firstly, notice that the macro-spin approximation and Eq. (6) are in excellent agreement. Also, there is nearly a perfect overlap of $l_{x,y}$ and m_z with the atomistic spin dynamics simulations when PBCs are used (Fig. 2(b,d,f)). However, quantitative deviations are seen when comparing to the atomistic spin dynamics simulations of a finite sized device (Fig. 2(a,c,e)), meaning that for this device-size the rotation is not perfectly coherent. In this case the deviations are not severe, so we can safely use Eq.(6). Further, we find that the higher the α the better the correspondence with the atomistic simulations of the finite sized device.

Relying on Eq. (6) we now investigate the final angle ϕ as a function of $|\mathbf{H}^{\text{SO}}|$ and τ_p for current pulses $\mathbf{j} \parallel \hat{\mathbf{x}}$ (i.e. a single switch event). The starting condition is for $\phi = 0$ ($\mathbf{l} = (1, 0)$). Results are shown in Fig. 2(g,h) for dampings $\alpha = 0.001$ and $\alpha = 0.01$; a very narrow region of overshoot (Fig. 2(g)) occurs in the underdamped case ($\alpha = 0.001$) for these ranges of $|\mathbf{H}^{\text{SO}}|$ ($0 < |\mathbf{j}| \leq 10^8 \text{ A/cm}^2$) and τ_p . For $\alpha = 0.01$ no overshoot is observed (Fig. 2(h)). For a device, a critical parameter is the minimum excitation strength required to write. This, we define as the SO-field required to bring \mathbf{l} just over $\phi = \pi/4$, denoted $|\mathbf{H}_C^{\text{SO}}|$. Applying Eq.(6), we calculate $|\mathbf{H}_C^{\text{SO}}|$ as a function of τ_p for square and triangular pulses considering several α . Figs. 3(a,b) show results for two dampings. At short pulse-durations, a $1/\tau_p$ dependence can be seen, showing smaller $|\mathbf{H}_C^{\text{SO}}|$ the lower the α . There is however a minimum $|\mathbf{H}_C^{\text{SO}}|$ -value which is α -independent: invoking $m_z \approx -\frac{1}{2\omega_e} \dot{\phi}$ and inserting into Eq. (6) gives a torque balance equation such that $\frac{dm_z}{dt} + 2\omega_e \alpha m_z = \frac{\omega_4}{4} \sin(4\phi) - \gamma H_y^{\text{SO}} \cos(\phi)$. In the limit of long τ_p with low current amplitude and/or long pulse rise-times, $dm_z/dt \approx 0$ and $2\omega_e \alpha m_z$ is small compared to the anisotropy and SO-field torques. Thus $\frac{\omega_4}{4} \sin(4\phi) - \gamma H_y^{\text{SO}} \cos(\phi) \approx 0$. As the requirement for a switch is that \mathbf{l} just overcomes the anisotropy barrier, it suffices to find the smallest H_y^{SO} on the interval $0 \leq \phi \leq \pi/4$, whereby $\gamma H_y^{\text{SO}} \cos(\phi) \geq \frac{\omega_4}{4} \sin(4\phi)$ is satisfied. This yields the lower limit for $H_y^{\text{SO}} = 27.2$ Oe ($1.36 \times 10^7 \text{ A/cm}^2$), which is in excellent agreement to the limits observed in Fig. 3 (horizontal dashed red line).

We now investigate the effect of finite pulse rise and fall times, τ_r , τ_f , respectively by trapezoidal pulses (as defined in Fig. 4) where $\tau_r = \tau_f$ and τ_p . $|\mathbf{H}_C^{\text{SO}}|$ is then calculated according to Eq. (6) as a function of the ratio τ_r/τ_p , considering four different τ_p . In Fig. 4(a) results are shown for $\alpha = 0.01$ and in Fig. 4(b), $\alpha = 0.005$. As can be seen, as far as $|\mathbf{H}_C^{\text{SO}}|$ is concerned, the dependence on τ_r/τ_p is not severe. Thus, in a real de-

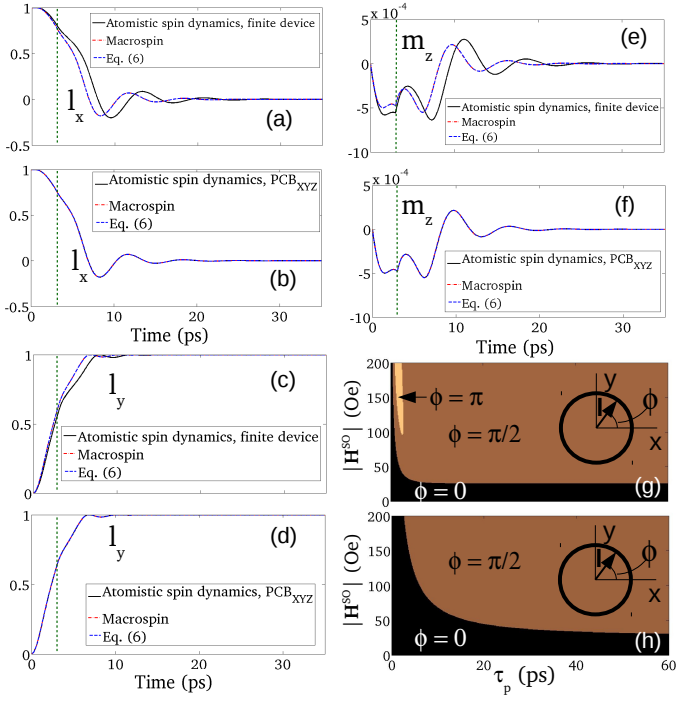


FIG. 2. (Color online) (a-f): Correspondence between atomistic spin dynamics, macro-spin modeling and Eq. (6) when comparing to the finite size device used in Fig.1 and when imposing PBCs along x, y, z using $150 \times 150 \times 5$ unit cells. (a,b) l_x vs time, (c,d) l_y vs time, (e,f) m_z vs time. The green vertical dashed lines mark the off-point of the pulse. (g,h): Final angle of \mathbf{l} as a function of $|\mathbf{H}_C^{\text{SO}}|$ and τ_p for $\alpha = 0.001$ (g) and $\alpha = 0.01$ (h). Square pulses have been used in all cases.

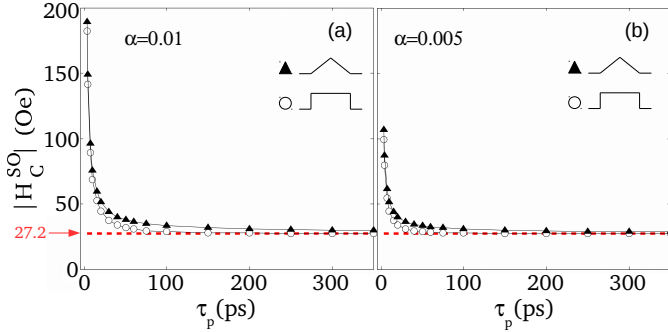


FIG. 3. (Color online) (a,b): $|\mathbf{H}_C^{\text{SO}}|$ vs. τ_p for different $\alpha = 0.01$ (a) and $\alpha = 0.005$ (b). The red dotted line and arrow mark the theoretically lowest $|\mathbf{H}_C^{\text{SO}}|$. A triangular pulse means that the rise and fall-times equals the pulse duration as defined in Fig. 4.

vice, pulse-shaping is not crucial to achieve a switching event while keeping injected current magnitudes at a feasible level; e.g. even a $\tau_r = \tau_p = 10$ ps (triangular) pulse can switch the device with $|\mathbf{H}_C^{\text{SO}}| \sim 45\text{--}60$ Oe, meaning $\sim 2.25\text{--}3 \times 10^7 \text{ A/cm}^2$ if $\alpha = 0.005\text{--}0.01$. The reason for a higher $|\mathbf{H}_C^{\text{SO}}|$ as τ_r/τ_p increases is a lower maximum amplitude m_z . The result is a reduced exchange torque.

In terms of the switching time, τ_s , defined here as the time it takes for l_y to reach 90% of its maximum value of 1, the difference can be significant. Fig. 4(c,d) show τ_s versus $|\mathbf{H}_C^{\text{SO}}|$ for three τ_r/τ_p -values under a current pulse of $\tau_p = 10$ ps. Here two cases are shown in terms of damping; $\alpha = 0.01$ and $\alpha = 0.005$. As long as one is reasonably above $|\mathbf{H}_C^{\text{SO}}|$, the behaviour is fairly consistent, with a doubling of the switching time as τ_r/τ_p approaches 1. The cause is the same as for $|\mathbf{H}_C^{\text{SO}}|$ although the effect of lower exchange torque is felt throughout the whole switch event (in determining $|\mathbf{H}_C^{\text{SO}}|$ only the time between $0 \leq \phi \leq \pi/4$) is relevant. For application point of view, however, the increase in τ_s may not be critical as all switching times are still in the picosecond regime.

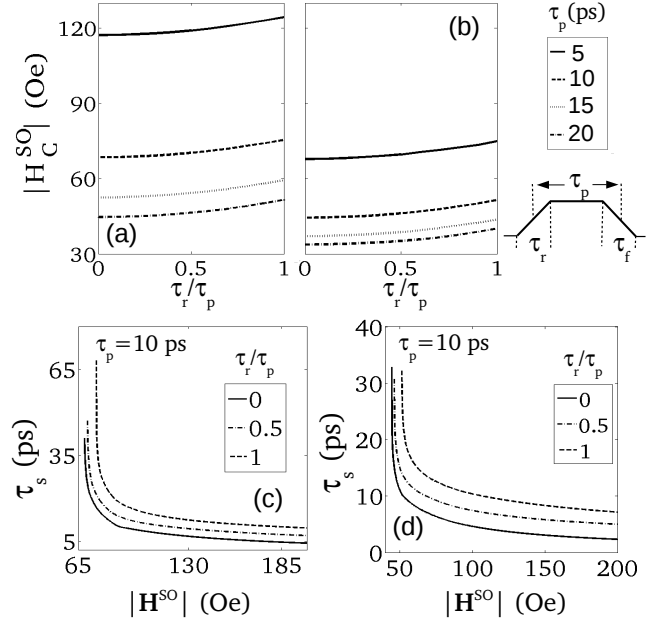


FIG. 4. (a,b): Dependence of $|\mathbf{H}_C^{\text{SO}}|$ on τ_r/τ_p for different values of τ_p and α ; $\alpha = 0.01, 0.005$ in (a),(b), respectively. The legend for (a,b) and pulse shape specification is shown to the right ($\tau_r/\tau_p = 0$ means a square pulse and $\tau_r/\tau_p = 1$ is a triangular pulse). (c,d): τ_s versus $|\mathbf{H}_C^{\text{SO}}|$ for different τ_r/τ_p and a fixed $\tau_p = 10$ ps. In (c), $\alpha = 0.01$ and in (d), $\alpha = 0.005$.

In conclusion, we have computationally shown reliable picosecond writing in antiferromagnetic systems whose symmetry allows for current-induced staggered SO-fields. A minimal risk of overshoot due to the field-like torque offers an advantage over structures relying on the anti-damping torque. Conditions for the lower limit of the switching field has been found. $|\mathbf{H}_C^{\text{SO}}|$ has a rather weak dependence on the rise/fall-time of the excitation while τ_s can increase up to a factor of two as the pulse shape goes from rectangular to triangular. The switching times are still in the picosecond time regime. Thus the device remains ultrafast also for non-square pulse shapes.

P. E. Roy and R. Otxoa contributed equally to this work.

* per24@cam.ac.uk

† ro274@cam.ac.uk

- [1] A. V. Kimel, B. A., Ivanov, R. V. Pisarev, A. Kirilyuk and Th. Rasing, *Nat. Phys.*, **320**, 727 (2009).
- [2] A. V. Kimel, A. Kirilyuk, P. A. Usachev, R. V. Pisarev and Th. Rasing, *Nature*, **435**, 655 (2005).
- [3] S. Wienholdt, D. Hinzke and U. Nowak, *Phys. Rev. Lett.*, **108**, 247207 (2012).
- [4] Ran. Cheng, Matthew W. Daniels, Jiang-Gang-Zhu and Di Xiao, *Phys. Rev. B.*, **91**, 064423 (2015).
- [5] Helen V. Gomonay and Vadim M. Loktev, *Phys. Rev. B.*, **81**, 144427 (2010).
- [6] E. V. Gomonay and V. M. Loktev, *Low Temperature Physics*, **40**, 17 (2014).
- [7] Ran Cheng and Qian Niu, *Phys. Rev. B.*, **89**, 081105(R) (2014).
- [8] A. C. Swaving and R. A. Duine, *Phys. Rev. B.*, **83**, 054428 (2011).
- [9] Erlend G. Tveten, Alireza Qaiumzadeh, O. A. Treiakov and Arne Braatas, *Phys. Rev. Lett.*, **110**, 127208 (2013).
- [10] Kjetil M. D. Hals, Yaroslav Tserkovnyak and Arne Braatas, *Phys. Rev. Lett.*, **106**, 107206 (2011).
- [11] J. Zelenzny, H. Gao, K. Vyborny, J. Zemen, J. Masek, Aurelien Manchon, J. Wunderlich, Jairo Sinova and T. Jungwirth, *Phys. Rev. Lett.*, **113**, 157201 (2014).
- [12] S. D. Ganichev, *Int. J. Mod. Phys. B.*, **22**, 1 (2008).
- [13] Sergii Khmelevskiy and Peter Mohn, *Appl. Phys. Lett.*, **93**, 162503 (2008).
- [14] A. B. Schick, S. Khmelevskiy, O. N. Mryasov, J. Wunderlich and T. Jungwirth, *Phys. Rev. B.*, **81**, 212409 (2010).
- [15] V. M. T. S. Barthem, C. V. Colin, H. Mayaffre, M. -H. Julien and D. Givord, *Nat. Commun.*, **4**, 2892 (2013).
- [16] Han-Chun, Zhi-Min Liao, R. G. Sumesh Sofin, Gen Feng, Xin-Mei Ma, Alexander B. Shick, Oleg N. Mryasov and Igor V. Shvets, *Adv. Mater.*, **24**, 6374 (2012).
- [17] F. Maca, J. Masek, O. Stelmakhovych, X. Marti, H. Reichlova, K. Uhlirova, P. Beran, P. Wadley, V. Novak and T. Jungwirth, *J. Magn. Magn. Mater.*, **324**, 1606 (2012).
- [18] P. Wadley *et al.*, *Nat. Commun.*, **4**, 2322 (2013).
- [19] P. Wadley *et al.*, *Science*, **351**, 587 (2016).
- [20] M. Jourdan, H. Brauning, A. Sapozhnik, H. -J. Elmers, H. Zabel and M. Klau, *J. Phys. D: Appl. Phys.*, **48**, 385001 (2015).
- [21] P. Wells and J. H. Smith, *Acta Cryst.*, **A26**, 379, 1970.
- [22] Vitoria M. T. S. Barthem, Claire V. Colin, Richard Haettel, Didier Defeu, Dominique Givord, *J. Magn. Magn. Mater.*, **406**, 289 (2016).
- [23] R. F. L. Evans, W. J. Fan, P. Chureemart, T. A. Ostler, M. O. A. Ellis and R. W. Chantrell, *J. Phys.: Condens. Matter* **26**, 103202 (2014).
- [24] R. Masrour, E. K. Hlil, M. Hamedoun, A. Benyoussef, A. Bouahar, H. Lassri, *J. Magn. Magn. Mater.*, **393**, 600 (2015).
- [25] J. Miltat, G. Albuquerque, and A. Thiaville, *Spin Dynamics in Confined Magnetic Structures I*, Topics in Applied Physics Vol. 83, edited by B. Hillebrands and K. Ounadjela Springer-Verlag, Berlin, 2002, Chapter 1.
- [26] W. H. Press, B. P. Flannery, S. A. Teukolsky, and W. T. Vetterling, *Numerical Recipes: The Art of Scientific Computing*, Cambridge University Press, Cambridge, England, 1988.